

Exciton behavior under the influence of metal nanoparticle near fields: Significance of nonlocal effects

Harini Hapuarachchi,^{1,*} Sarath D. Gunapala,² Qiaoliang Bao,³ Mark I. Stockman,⁴ and Malin Premaratne^{1,†}

¹*Advanced Computing and Simulation Laboratory (A χ L), Department of Electrical and Computer Systems Engineering, Monash University, Clayton, Victoria 3800, Australia*

²*Jet Propulsion Laboratory, California Institute of Technology, Pasadena, California 91109, USA*

³*Department of Materials Science and Engineering, Monash University, Clayton, Victoria 3800, Australia*

⁴*Department of Physics and Astronomy, Georgia State University, Atlanta, Georgia 30303, USA*



(Received 18 June 2018; revised manuscript received 22 August 2018; published 18 September 2018)

We analytically characterize the influence of a neighboring metal nanoparticle (MNP) on the behavioral trends of a quantum dot (QD) using a generalized nonlocal optical response (GNOR) method based approach, taking the MNP distance dependent modifications to the QD population relaxation and dephasing rates into account. The GNOR model is a recent generalization and an extension of the hydrodynamic Drude model (HDM), which goes beyond HDM by taking into account both the convection current and electron diffusion in the MNPs. It allows unified theoretical explanation of some experimentally observed plasmonic phenomena which otherwise would require *ab initio* analysis as the conventional local response approximation (LRA) fails to account for them. For example, it has been demonstrated in literature that the GNOR model captures size dependent resonance shifts of small MNPs which are unrevealed by the conventional LRA based methods, and it has proven to yield results displaying better agreement with the experimental observations for plasmonic experiments. Attempts to incorporate MNP nonlocal effects in the analytical characterization of vicinal excitons found in literature utilize the phenomenological hydrodynamic model and assume the absence of MNP interband effects. Moreover, they are only applicable to narrow parameter regions. In this paper we present a complete analytical characterization which overcomes these drawbacks and lends to the perusal of the system over wide continua of various parameters, enabling us to get an elevated view at a much lesser level of complexity compared to the conventional LRA based numerical methods or the conventional *ab initio* methods of accounting for the nonlocal effects. Our proposed GNOR based model predicts strong modifications to various QD properties such as population difference, absorption, MNP induced shifts to excitonic energy and Förster enhanced broadening, coherent plasmonic field enhancement, and quantum state purity, compared to the conventional LRA based predictions. Such modifications are prominent with small MNP radii, high QD dipole moments, small detunings (of the coherent external illumination from the bare excitonic resonance), and near parameter regions exhibiting plasmonic meta resonance (PMR)-like behavior. Moreover, our complete analytical characterization enables optimization of the large system parameter space for different applications, a luxury not fully offered by the methods currently available in literature.

DOI: [10.1103/PhysRevB.98.115430](https://doi.org/10.1103/PhysRevB.98.115430)

I. INTRODUCTION

Luminescent semiconductor nanocrystals or quantum dots (QDs) are a class of nanomaterials possessing unique photophysical properties such as high quantum yield and exceptional resistance to both photobleaching and chemical degradation [1]. Ability to exploit the unique optics of QDs has a broad range of applications in optoelectronic devices such as high-efficiency single photon sources, quantum information processors, light emitting devices, photovoltaic cells, optoelectronic nanoswitches, various in-vivo nanodevices [2–7], and as zero-index gain media [8] of spasers [9–15]. In such applications, the optical properties of the excitons in the QDs

can be controlled using different reservoirs such as optical microresonators or photonic crystal nanocavities [2,7,16–21]. However, the size of such resonators has an intrinsic limitation which inhibits device miniaturization beyond the diffraction limit of infrared light [2].

Metal nanoparticles (MNPs) possess nanocavitylike near fields that can amplify and localize electromagnetic fields at nanometer length scales much smaller than the diffraction limit of light, due to the existence of localized surface plasmon resonances (LSPRs) [22–31], which are formed primarily due to the collective motion of the conduction band electrons tightly bound to a metal-insulator interface [23,32]. Thus, MNPs can be used to tailor the optical properties of QDs at nanoscale [33,34].

Almost all recent studies of QDs subjected to near fields of MNP nanocavities [2,7,34–39] deploy the local response approximation (LRA) [40] to model the MNP. In the LRA,

*harini.hapuarachchi@monash.edu

†malin.premaratne@monash.edu

the nonlocal effects of the MNP's optical response are not taken into consideration and it has recently been challenged on a number of accounts; one example being its prediction that the resonance energy of the LSPRs in the quasistatic limit is independent of the MNP size [40]. This claim by LRA conflicts with the experimentally observed results [40–44]. The experimentally observed size dependence of the LSPR energy is believed to be a result of the quantum properties of the MNP's free electron gas, which strengthen as the particles lessen in size [45]. Modeling the MNP based on *ab initio* approaches such as density-functional theory (DFT) [46] captures such nonclassical effects [47,48]. However, such approaches are computationally quite demanding. Simpler and computationally less demanding approach would be to surpass the LRA using nonlocal response theories such as the nonlocal hydrodynamic or the generalized nonlocal optical response (GNOR) models [40,49]. Combining such analytical nonlocal models with a fully analytical characterization of the excitons in a neighboring QD enables the generation of insightful analytical results and the optimization of the large parameter space associated with device designing, a functionality not fully offered by the methods currently available in literature.

When a metal nanoparticle is made increasingly smaller, the ratio of the number of surface atoms to those that make up the bulk of the particle grows larger. This causes the surface effects to dominate the physics of the particle [50]. It has been shown that the origin of the size dependence in nonlocal response is the smearing of the surface charges induced by an external electric field over a finite distance (few Å) into the metal via the presence of longitudinal waves. However, in the LRA, it is assumed that the charges induced due to an external field reside only on the geometric surface of a metal structure [40]. Thus, nanoplasmonics experiments defy explanations with classical LRA [40–44] due to the nonclassical effects arising as a result of the nonlocal response.

The concept of nonlocal response in MNPs was first introduced phenomenologically, and was based on the semiclassical hydrodynamic Drude model (HDM) afterwards. The generalized nonlocal optical response (GNOR) model is a recent generalization and an extension of the HDM model, which goes beyond HDM by taking into account both the convection current and electron diffusion phenomena in the MNPs [41]. Thus, it better captures both size dependent resonance shifts and linewidth broadening of the extinction cross section that occur as the radius of the MNP decreases. Experiments on dimers with few nanometer sized gaps have suggested that the GNOR model yields results similar to the experimentally measured spectra, without the need of invoking the quantum mechanical effect of tunneling [40].

First-principle approaches such as variants of density-functional theory (DFT) [47,51,52] are capable of describing microscopic interaction effects of electrons in metals with high accuracy. However, *ab initio* quantum mechanical treatment of the optical properties of plasmonic systems is quite demanding, due to the high number of electrons contributing to their optical response. Such models are usually limited to very small systems with a few thousand conduction electrons. However, a practical plasmonic system used in experiments contain many millions or even billions of electrons which

can be barely handled with first-principle methods [52]. The GNOR model allows unified explanations of observed experimental phenomena for both monomers and dimers which previously seemed to require *ab initio* explanations [40,41] at an extremely lesser level of computational complexity.

In this paper we study the behavior of excitons under the influence of MNP near fields associated with LSPRs [53,54] by modeling the MNP using a generalized nonlocal optical response (GNOR) method based fully analytical approach. Our main objective is to highlight how the incorporation of the MNP's nonlocal effects change the optical properties observed in the excitons of vicinal QDs. Our results suggest that significant differences exist between the LRA and GNOR based predictions, especially for QDs with high dipole moments near small MNPs at the incidence of coherent external illumination with small detunings from the bare excitonic resonance and in the parameter regimes exhibiting near plasmonic meta resonance (PMR)-like [6] behavior.

This paper is organized as follows. In Sec. II A we model the exciton of the QD as an open quantum system which undergoes dipole interaction with the externally incident coherent driving field and the near field of the LSPRs, taking the nonlocal effects of the MNP into account using a GNOR based approach. In Sec. II B we analytically solve the system using Cardano's method. In Sec. III we present a tabulation of the complete QD characterization under the influence of the MNP, followed by a detailed analysis and a discussion of the system (in Sec. IV) using the aforementioned analytical characterization.

II. FORMALISM

A. The open quantum system

Let us consider an MNP-QD hybrid nanosystem comprising of an MNP with radius a and a QD with a relatively negligible radius, separated by a distance R , as depicted in Fig. 1. Throughout the formalism section we use bold fonts, hat notation, tilde notation, and bolded hat notation to refer to vectors, quantum mechanical operators, slowly varying amplitudes, and unit vectors, respectively.

The system is submerged in an environment of relative permittivity ϵ_b and experiences an externally applied coherent electric field $\mathbf{E} = \hat{z}E_0(e^{-i\omega t} + e^{i\omega t})/2 = \hat{z}E$, where i is the imaginary unit, ω is the angular frequency, and \hat{z} is a unit vector along or perpendicular to the MNP-QD axis. All distances are assumed small enough for the retardation effects to be ignored and thermal effects [55,56] are assumed to be negligible in the model.

We choose the direction of the incident field to be parallel/perpendicular to the axis of the MNP-QD system. QD is considered as a spherical semiconductor with a dielectric constant ϵ_s containing a two-level atomlike quantum system (exciton) at the center. The exciton is treated quantum mechanically, using the density matrix formalism, with bare excitonic energy $\hbar\omega_0$ and transition dipole moment μ_d .

The dielectric permittivity of the MNP is obtained using the Drude-like dielectric function [40] $\epsilon_m(\omega) = \epsilon_{\text{core}}(\omega) - \omega_p^2/\omega(\omega + i\gamma)$, where ω_p is the bulk plasmon frequency, γ is the relaxation constant of the bulk material, and $\epsilon_{\text{core}}(\omega)$ is the response from the bound electrons [40]. We can safely assume

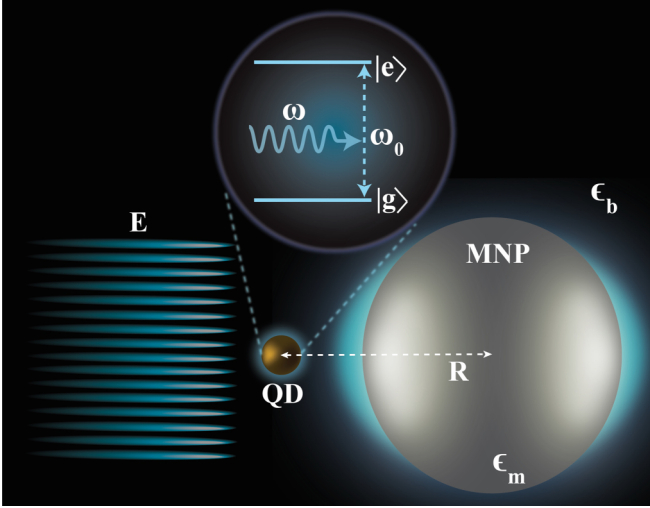


FIG. 1. The schematic diagram of the system under study. The exciton in the quantum dot (QD) undergoes dipole interaction with the coherent external drive E (with angular frequency ω) and the near field of the localized surface plasmon resonances in the metal nanoparticle (MNP). The bare excitonic energy of the QD is $\hbar\omega_0$. The MNP-QD center separation distance is R . The dielectric permittivities of the MNP and the host medium are ϵ_m and ϵ_b , respectively.

that $\epsilon_{\text{core}} = 1$ in cases where interband effects are absent and only the conduction band electrons contribute to the optical properties of the material. However, in common plasmonic material such as gold and silver, interband transitions play an important role in determining the plasmonic response. Therefore, in our analysis, we determine ϵ_{core} using the recipe $\epsilon_{\text{core}} = \epsilon_{\text{expt}}(\omega) + \omega_p^2 / [\omega(\omega + i\gamma)]$ [40], where ϵ_{core} can be determined using an experimentally measured bulk dielectric function, such as the data set presented by Johnson and Christy [57].

Let $\hat{a} = |g\rangle\langle e|$ and $\hat{a}^\dagger = |e\rangle\langle g|$ be the exciton creation and annihilation operators, where $|g\rangle$ and $|e\rangle$ are the energy eigenvectors of the unperturbed atomic Hamiltonian representing the exciton ground and excited states, respectively. The Hamiltonian of the QD under the influence of the MNP and the externally applied electric field can be given as [5,35,58,59]

$$\hat{\mathcal{H}}_{\text{qd}} = \hbar\omega_0 \hat{a}^\dagger \hat{a} - E_{\text{qd}} \mu_d (\hat{a} + \hat{a}^\dagger), \quad (1)$$

where E_{qd} is the (magnitude of) the total electric field experienced by the exciton at the center of QD. E_{qd} comprises the influence of the externally incident coherent illumination E and the dipole response field of the vicinal MNP at the QD location given by [54] $E_{\text{res}} = s_\alpha P_{\text{mnp}} / (4\pi\epsilon_0\epsilon_b R^3)$, where ϵ_0 denotes the free space permittivity and $s_\alpha = 2(-1)$ is an orientation parameter which indicates that the external field is parallel (perpendicular) to the axis connecting the MNP and QD centers. The field experienced by the quantum system at the center of the QD will be screened due to ϵ_s such that [35] $E_{\text{qd}} = (E + E_{\text{res}}) / \epsilon_{\text{effS}}$, where $\epsilon_{\text{effS}} = (2\epsilon_b + \epsilon_s) / 3\epsilon_b$. Magnitude of the MNP polarization denoted by P_{mnp} is given by [50]

$$P_{\text{mnp}} = 4\pi\epsilon_0\epsilon_b a^3 (\beta \tilde{E}_{\text{mnp}}^+ e^{-i\omega t} + \beta^* \tilde{E}_{\text{mnp}}^- e^{i\omega t}), \quad (2)$$

where \tilde{E}_{mnp}^+ and \tilde{E}_{mnp}^- are the positive and negative frequency coefficients of E_{mnp} , which is the electric field felt by the MNP, given by

$$E_{\text{mnp}} = E + \frac{1}{4\pi\epsilon_0\epsilon_b} \frac{s_\alpha P_{\text{qd}}}{\epsilon_{\text{effS}} R^3}, \quad (3)$$

with the QD polarization denoted as $P_{\text{qd}} = \mu_d(\rho_{12} + \rho_{21})$ [36], using the off-diagonal density matrix elements ρ_{12} and ρ_{21} of the QD. Both MNP and QD polarize along the incoming radiation E .

In this work we model β , the Clausius Mossotti factor of the MNP, using the generalized nonlocal optical response (GNOR) method [40] in contrast to the traditional local response approximation (LRA) usually adopted in literature [6,35,50,60,61]. In the GNOR based approach, β is obtained as follows [40]:

$$\beta = \frac{\epsilon_m(\omega) - \epsilon_b(1 + \delta_{\text{NL}})}{\epsilon_m(\omega) + 2\epsilon_b(1 + \delta_{\text{NL}})}, \quad (4)$$

where the nonlocal correction δ_{NL} is given by

$$\delta_{\text{NL}} = \frac{\epsilon_m(\omega) - \epsilon_{\text{core}}(\omega)}{\epsilon_{\text{core}}(\omega)} \frac{j_1(k_L a)}{k_L a j_1'(k_L a)}. \quad (5)$$

The spherical Bessel function of the first kind of angular-momentum order 1 is denoted by j_1 and j_1' is its first order differential with respect to the argument. The longitudinal wave vector k_L that is responsible for the nonlocal effects in the MNP is modeled in the GNOR based approach as $k_L^2 = \epsilon_m(\omega) / \xi_{\text{GNOR}}^2(\omega)$. The frequency dependent function $\xi_{\text{GNOR}}(\omega)$, namely the nonlocal parameter of the GNOR model, is given by

$$\xi_{\text{GNOR}}^2(\omega) = \frac{\epsilon_{\text{core}}(\omega)[\kappa^2 + D(\gamma - i\omega)]}{\omega(\omega + i\gamma)}, \quad (6)$$

where D is the diffusion constant of the GNOR model and $\kappa^2 = (3/5)v_F^2$ for $\omega \gg \gamma$ (in the high frequency limit) with v_F being the MNP Fermi velocity. To obtain the relevant equations for the HDM model, one can simply replace $\xi_{\text{GNOR}}^2(\omega)$ by the nonlocal parameter in the HDM model given by $\xi_{\text{HDM}}^2(\omega) = \epsilon_{\text{core}}(\omega)\kappa^2 / [\omega(\omega + i\gamma)]$ [40].

We factor out the high frequency time dependence of the off-diagonal density matrix elements of the QD as [50] $\rho_{12} = \tilde{\rho}_{12} e^{i\omega t}$ and $\rho_{21} = \rho_{12}^*$. Using these definitions, E_{qd} can be recast as

$$E_{\text{qd}} = \frac{\hbar}{\mu_d} \{ \Omega_{12}^{\text{eff}} + \eta \tilde{\rho}_{21} \} e^{-i\omega t} + \text{H.c.} = \tilde{E}_{\text{qd}}^+ e^{-i\omega t} + \text{H.c.}, \quad (7)$$

where H.c. stands for Hermitian conjugate.

The Rabi frequency in the absence of quantum coherence is denoted by Ω_{12}^{eff} [61] and η arises due to the MNP electric field component induced as a result of the QD dipole response field incident on the MNP, and hence can be thought of as the self-interaction of the QD [50]. These quantities are given by

$$\Omega_{12}^{\text{eff}} = \Omega_{12}^0 \left(1 + \frac{s_\alpha \beta a^3}{R^3} \right), \quad (8a)$$

$$\eta = \frac{s_\alpha^2 \beta a^3 \mu_d^2}{4\pi\epsilon_0\epsilon_b \hbar \epsilon_{\text{effS}}^2 R^6}, \quad (8b)$$

where $\Omega_{12}^0 = (\mu_d E_0)/(2\hbar\epsilon_{\text{effs}})$ is the Rabi frequency of the bare external field when the MNP and QD are isolated (large R).

We obtain the effective or normalized Rabi frequency [21,62] of the QD under the influence of both MNP and the external field using the effective field incident on the QD exciton given by (7) as [61] $\Omega_{12}^r = (\mu_d/\hbar)\tilde{E}_{\text{qd}}^+ = \Omega_{12}^{\text{eff}} + \eta\tilde{\rho}_{21}$, where \tilde{E}_{qd}^+ is the positive frequency coefficient of E_{qd} . Using the Rabi frequencies under bare external illumination and in the presence of the MNP, the coherent plasmonic field enhancement (CPFE) experienced by the excitonic system in the QD is defined as [6,7] CPFE = $|\Omega_{12}^r/\Omega_{12}^0|^2$.

The Hamiltonian of the QD given by Eq. (1) describes a closed quantum system where the effects of the environment are not yet taken into account. The QD couples with the environment, forming an open quantum system with irreversible dynamics [54]. Quantum dynamics of the system coupled with the environments can be accounted for by solving the following master equation for the QD density matrix $\hat{\rho}$ [50]:

$$\dot{\hat{\rho}} = \frac{i}{\hbar}[\hat{\rho}, \hat{\mathcal{H}}_{\text{qd}}] + \lambda_1 \mathcal{L}(\hat{a})\hat{\rho} + \lambda_2 \mathcal{L}(\hat{a}^\dagger)\hat{\rho} + \lambda_3 \mathcal{L}(\hat{a}^\dagger\hat{a})\hat{\rho}, \quad (9)$$

$$\dot{\hat{\rho}} = \frac{i}{\hbar} \begin{bmatrix} -\mu_d E_{\text{qd}}(\rho_{12} - \rho_{21}) & -\mu_d E_{\text{qd}}(\rho_{11} - \rho_{22}) + \hbar\omega_0\rho_{12} \\ -\mu_d E_{\text{qd}}(\rho_{22} - \rho_{11}) - \hbar\omega_0\rho_{21} & -\mu_d E_{\text{qd}}(\rho_{21} - \rho_{12}) \end{bmatrix} - \begin{bmatrix} 2\lambda_2\rho_{11} - 2\lambda_1\rho_{22} & (\lambda_1 + \lambda_2 + \lambda_3)\rho_{12} \\ (\lambda_1 + \lambda_2 + \lambda_3)\rho_{21} & 2\lambda_1\rho_{22} - 2\lambda_2\rho_{11} \end{bmatrix}, \quad (11)$$

where the latter component is the relaxation matrix $\Gamma(\hat{\rho})$ of the quantum system. For optical frequencies, $\lambda_2 \approx 0$ even near room temperature [50]. Let

$$\tau = 1/(2\lambda_1), \quad (12a)$$

$$T = 1/(\lambda_1 + \lambda_3). \quad (12b)$$

Using (12a), (12b), and $\rho_{11} + \rho_{22} = 1$,

$$\Gamma(\hat{\rho}) \approx \begin{bmatrix} (\rho_{11} - 1)/\tau & \rho_{12}/T \\ \rho_{21}/T & \rho_{22}/\tau \end{bmatrix}, \quad (13)$$

where ρ_{uv} refers to the density matrix element located at the u th row and v th column. Therefore, the master equation can be approximated using (13) for optical frequencies of our interest as

$$\dot{\hat{\rho}} = \frac{i}{\hbar}[\hat{\rho}, \hat{\mathcal{H}}_{\text{qd}}] - \Gamma(\hat{\rho}). \quad (14)$$

The energy or population relaxation time of the QD which will lead to a mixing between ρ_{11} and ρ_{22} is denoted by τ . The relaxation time τ includes a contribution from nonradiative decay to the dark states [63]. T refers to the polarization relaxation or dephasing time [6,64] which will cause losses in the off-diagonal density matrix elements of the QD. Both population relaxation and dephasing cause loss of coherence in the system [50].

The normalized decay rates in the vicinity of the MNP can be expressed as follows, taking the nonlocal effects of the MNP into account, according to the two linearly independent

where the three Lindblad terms $\lambda_1 \mathcal{L}(\hat{a})\hat{\rho}$, $\lambda_2 \mathcal{L}(\hat{a}^\dagger)\hat{\rho}$, and $\lambda_3 \mathcal{L}(\hat{a}^\dagger\hat{a})\hat{\rho}$ correspond to the bath induced decay of the excitonic excited state into the ground state, bath induced excitation of the system into the excitonic excited state, and elastic scattering processes between the bath and the quantum system, respectively. As the elastic scattering processes conserve the number of excitations in the bath and the atom separately, we assume it gives rise to pure dephasing in the quantum system which is analogous to T_2 relaxation in nuclear magnetic resonance (NMR) [50].

Expansion of Lindblad terms in (9) as $\mathcal{L}(\hat{A})\hat{\rho} = 2\hat{A}\hat{\rho}\hat{A}^\dagger - \hat{A}^\dagger\hat{A}\hat{\rho} - \hat{\rho}\hat{A}^\dagger\hat{A}$ results in

$$\begin{aligned} \dot{\hat{\rho}} = \frac{i}{\hbar} & [\hat{\rho}, \hat{\mathcal{H}}_{\text{qd}}] + \lambda_1(2\hat{a}\hat{\rho}\hat{a}^\dagger - \hat{a}^\dagger\hat{a}\hat{\rho} - \hat{\rho}\hat{a}^\dagger\hat{a}) \\ & + \lambda_2(2\hat{a}^\dagger\hat{\rho}\hat{a} - \hat{a}\hat{a}^\dagger\hat{\rho} - \hat{\rho}\hat{a}\hat{a}^\dagger) \\ & + \lambda_3(2\hat{a}^\dagger\hat{a}\hat{\rho}\hat{a}^\dagger\hat{a} - \hat{a}^\dagger\hat{a}\hat{\rho} - \hat{\rho}\hat{a}^\dagger\hat{a}), \end{aligned} \quad (10)$$

where we have used the property $(\hat{a}^\dagger\hat{a})(\hat{a}^\dagger\hat{a}) = \hat{a}^\dagger\hat{a}$ for $\hat{a} = |g\rangle\langle e|$ and $\hat{a}^\dagger = |e\rangle\langle g|$.

Matrix form of the master equation (10) in the basis space formed by $|g\rangle, |e\rangle$ reads

orientations of the QD dipole moment [65,66]:

$$\left(\frac{1/\tau}{1/\tau_0}\right)_\perp = 1 + \frac{3}{2k^3} \sum_{n=1}^{\infty} \left[\frac{\text{Im}\{\alpha_n(\omega)\}(n+1)^2}{(a+R)^{2(n+2)}} \right], \quad (15a)$$

$$\left(\frac{1/\tau}{1/\tau_0}\right)_\parallel = 1 + \frac{3}{2k^3} \sum_{n=1}^{\infty} \left[\frac{\text{Im}\{\alpha_n(\omega)\}n(n+1)}{2(a+R)^{2(n+2)}} \right], \quad (15b)$$

where τ_0 is the population relaxation time of the QD in the absence of the MNP, $k = \omega/c$ is the wave number, α_n is the n th polarizability of the MNP, and \perp and \parallel denote the radial ($s_\alpha = 2$) and tangential ($s_\alpha = -1$) orientations of the QD dipole with respect to the MNP. Using the above equations, it can be shown that, in the dipole limit where $n = 1$ and $\alpha = \beta(\omega)a^3$, the QD relaxation time depends on the MNP nonlocal dipolar polarizability as

$$\tau(\omega) = \frac{\tau_0}{1 + f \text{Im}\{\alpha(\omega)\}/\{k^3(a+R)^6\}}, \quad (16)$$

where the factor $f = 6$ when $s_\alpha = 2$ and $f = 3/2$ when $s_\alpha = -1$. Using (12a), (12b), and $t_p = 1/\lambda_3$ where t_p corresponds to pure dephasing due to elastic scattering, the relationship between the QD dephasing rate and the MNP nonlocal dipolar polarizability can be arrived at as [64]

$$T(\omega) = \frac{2\tau(\omega)t_p}{t_p + 2\tau(\omega)}. \quad (17)$$

Using $R \rightarrow \infty$ in (16) and (17),

$$t_p = 2\tau_0 T_0 / (2\tau_0 - T_0). \quad (18)$$

B. Steady state analytical solution

As a majority of QD related applications operate well away from the rise time of the applied field where the transients have settled down [2,6,24,61], throughout this work we focus on the steady state solution of the system.

We first define the following to be used when solving the master equation (14),

$$\tilde{\rho}_{12} = \mathcal{A} + i\mathcal{B}, \quad (19a)$$

$$\tilde{\rho}_{21} = \mathcal{A} - i\mathcal{B}, \quad (19b)$$

$$\Delta = \rho_{11} - \rho_{22}, \quad (19c)$$

$$\Omega_{12}^{\text{eff}} = \Omega_{\text{re}} + i\Omega_{\text{im}}, \quad (19d)$$

$$\eta = \eta_{\text{re}} + i\eta_{\text{im}}. \quad (19e)$$

Using element-wise comparison on (14), we can arrive at the system Bloch equations defining the behavior of the QD under the influence of the MNP and the externally incident field,

$$\dot{\rho}_{22} = -\frac{\rho_{22}}{\tau(\omega)} + i\Omega_{12}^r \rho_{12} - i\Omega_{12}^{r*} \rho_{21}, \quad (20a)$$

$$\dot{\rho}_{11} = \frac{\rho_{22}}{\tau(\omega)} - i\Omega_{12}^r \rho_{12} + i\Omega_{12}^{r*} \rho_{21}, \quad (20b)$$

$$\dot{\tilde{\rho}}_{21} = -[i(\omega_0 - \omega) + 1/T(\omega)]\tilde{\rho}_{21} + i\Omega_{12}^r \Delta. \quad (20c)$$

By rearranging (20) using (19), we can arrive at the following form of the system Bloch equations:

$$\dot{\mathcal{A}} = -\frac{\mathcal{A}}{T(\omega)} + \delta\mathcal{B} - (\Omega_{\text{im}} + \eta_{\text{im}}\mathcal{A} - \eta_r\mathcal{B})\Delta, \quad (21a)$$

$$\dot{\mathcal{B}} = -\frac{\mathcal{B}}{T(\omega)} - \delta\mathcal{A} - (\Omega_{\text{re}} + \eta_{\text{re}}\mathcal{A} + \eta_{\text{im}}\mathcal{B})\Delta, \quad (21b)$$

$$\dot{\Delta} = \frac{1 - \Delta}{\tau(\omega)} + 4[\Omega_{\text{im}}\mathcal{A} + \Omega_{\text{re}}\mathcal{B} + \eta_{\text{im}}(\mathcal{A}^2 + \mathcal{B}^2)], \quad (21c)$$

where $\delta = \omega - \omega_0$ denotes the detuning of the external field with the QD excitonic transition.

In the steady state, using (21a) and (21b),

$$\begin{aligned} \mathcal{A} &= \frac{-[\delta\Omega_{\text{re}} + \Omega_{\text{im}}/T(\omega)]\Delta - (\eta_{\text{im}}\Omega_{\text{im}} + \Omega_{\text{re}}\eta_{\text{re}})\Delta^2}{[\eta_{\text{im}}\Delta + 1/T(\omega)]^2 + (\delta + \eta_{\text{re}}\Delta)^2} \\ &= -\text{Re}\left(\frac{\Omega_{12}^{\text{eff}}\Delta}{\delta + \eta\Delta + i/T(\omega)}\right), \quad (22) \\ \mathcal{B} &= \frac{[\delta\Omega_{\text{im}} - \Omega_{\text{re}}/T(\omega)]\Delta + (\eta_{\text{re}}\Omega_{\text{im}} - \Omega_{\text{re}}\eta_{\text{im}})\Delta^2}{[\eta_{\text{im}}\Delta + 1/T(\omega)]^2 + (\delta + \eta_{\text{re}}\Delta)^2} \\ &= \text{Im}\left(\frac{\Omega_{12}^{\text{eff}}\Delta}{\delta + \eta\Delta + i/T(\omega)}\right). \quad (23) \end{aligned}$$

Using (21c) in the steady state we can obtain [64]

$$w_3\Delta^3 + w_2\Delta^2 + w_1\Delta + w_0 = 0, \quad (24)$$

where

$$w_3 = T(\omega)^2(\eta_{\text{re}}^2 + \eta_{\text{im}}^2),$$

$$w_2 = 2T(\omega)^2\delta\eta_{\text{re}} + 2T(\omega)\eta_{\text{im}} - T(\omega)^2(\eta_{\text{re}}^2 + \eta_{\text{im}}^2),$$

$$w_1 = T(\omega)[4\tau(\omega)|\Omega_{12}^{\text{eff}}|^2 - 2\eta_{\text{im}}] + T(\omega)^2(\delta^2 - 2\delta\eta_{\text{re}}) + 1,$$

$$w_0 = -T(\omega)^2\delta^2 - 1.$$

Setting $\tilde{w}_i = w_i/w_3$ for $i = 0, 1$, and 2 we can obtain

$$\Delta^3 + \tilde{w}_2\Delta^2 + \tilde{w}_1\Delta + \tilde{w}_0 = 0. \quad (25)$$

Using Cardano's method for solving cubic equations [67] we obtain the three possible solutions for Δ as

$$\Delta_1 = (p_1 + p_2) - \tilde{w}_2/3, \quad (26a)$$

$$\Delta_2 = -(p_1 + p_2)/2 - \tilde{w}_2/3 + i\sqrt{3}(p_1 - p_2)/2, \quad (26b)$$

$$\Delta_3 = -(p_1 + p_2)/2 - \tilde{w}_2/3 - i\sqrt{3}(p_1 - p_2)/2. \quad (26c)$$

In the above equation

$$p_1 = \mathcal{P}_1^{1/3}, \quad \text{where } \mathcal{P}_1 = r + \sqrt{q^3 + r^2}, \quad (27a)$$

$$p_2 = \mathcal{P}_2^{1/3}, \quad \text{where } \mathcal{P}_2 = r - \sqrt{q^3 + r^2}, \quad (27b)$$

where $q = \tilde{w}_1/3 - \tilde{w}_2^2/9$ and $r = (\tilde{w}_1\tilde{w}_2 - 3\tilde{w}_0)/6 - \tilde{w}_2^3/27$.

As $\Delta = \rho_{11} - \rho_{22}$ is the QD population difference, only the real roots of Δ satisfying the condition $-1 \leq \Delta \leq 1$ are useful [64]. The first Cardano root of (25), Δ_1 , given by (26a), holds the only real root which readily satisfies this condition when $q^3 + r^2 \geq 0$, where we have easily picked the real cubic roots of \mathcal{P}_1 and \mathcal{P}_2 as p_1 and p_2 , respectively.

However, when $q^3 + r^2 < 0$, \mathcal{P}_1 possesses three complex cubic roots, the complex conjugates of which will appear as the cubic roots of \mathcal{P}_2 . Careful observation of (26) reveals that all three roots of Δ (Δ_1 , Δ_2 , and Δ_3) are real in such conditions. Under this condition, the physically valid root of Δ in (25) is given by Δ_1 in (26a) when the cubic roots of \mathcal{P}_1 and \mathcal{P}_2 are picked using De Moivre's n th root theorem for complex numbers as (see the Appendix)

$$p_1 = |\mathcal{P}_1|^{1/3}[\cos(\theta_1/3) + i\sin(\theta_1/3)] \quad \text{and} \quad p_2 = p_1^*, \quad (28)$$

where $\mathcal{P}_1 = |\mathcal{P}_1|/\theta_1$ in the polar form. The above analytical results were verified for a large parameter space against the steady state numerical solutions of (21), (22), and (23). Thus, the complete and physically valid analytical solution of (25) for the entire parameter region considered reads $\Delta = p_1 + p_2 - \tilde{w}_2/3$, where

$$p_1 = (\mathcal{P}_1)^{1/3} \in \mathbb{R} \quad \text{and} \quad p_2 = (\mathcal{P}_2)^{1/3} \in \mathbb{R} \quad \text{for } q^3 + r^2 \geq 0,$$

$$p_1 = |\mathcal{P}_1|^{1/3} \cos(\theta_1/3) \quad \text{and} \quad p_2 = p_1^* \quad \text{for } q^3 + r^2 < 0.$$

C. Absorption, energy, and dephasing rate normalization of the QD in the presence of the MNP

Variation of optical properties such as QD absorption, red and blueshifts of exciton energy, and dephasing rates in the presence of plasmonic nanocavities could be exploited for the development of nanoscale plasmonic devices particularly for chemical and biological sensing applications [2,61]. We now proceed to analytically characterize such QD properties using the GNOR based approach.

The energy absorption of the QD can be obtained using the QD population difference as [50]

$$Q_{\text{qd}} = \hbar\omega_0\rho_{22}/\tau(\omega) = \hbar\omega_0(1 - \Delta)/[2\tau(\omega)], \quad (29)$$

where we replace the conventional LRA based population difference with the newly suggested GNOR based Δ .

The system Bloch equation (20c) for the off-diagonal density matrix element ρ_{21} can be recast as

$$\dot{\rho}_{21} = -[i(\Pi_{21} - \omega) + \Lambda_{21}]\rho_{21} + i\Omega_{12}^{\text{eff}}\Delta. \quad (30)$$

The astute reader will notice that Π_{21} and Λ_{21} denote the normalized energy and the Förster-enhanced broadening (normalized dephasing rate) of the QD excitonic transition caused by the presence of the vicinal MNP [61] given by $\Pi_{21} = \omega_0 - \eta_{\text{re}}\Delta$ and $\Lambda_{21} = 1/T(\omega) + \eta_{\text{im}}\Delta$. We call the two factors $\Pi_f = \eta_{\text{re}}\Delta$ and $\Lambda_f = \eta_{\text{im}}\Delta$ the exciton transition energy (red) shift and FRET rate factor (or the dephasing rate blueshift), respectively.

D. Quantum state purity of the system

Recently there has been considerable progress in investigating the potential of using semiconductor quantum dots as qubits, where identifying and ameliorating sources of decoherence are important steps in understanding and improving system performance [68,69]. It has also been proposed that directed nanoscale information transfer can be achieved by coupling qubits, for example in QDs, to plasmonic nanostructures [36]. To exploit this paradigm, it is vital to understand the effects of MNP-QD coupling on the properties of QD, including how nonclassical phenomena such as the MNP nonlocal response could affect the quantum information. A GNOR based analytical characterization of the quantum state purity of the QD could be useful in this context.

A system's ability to exhibit quantum interference or "coherence" is a characteristic of a system in a pure quantum state that is maximally specified within quantum mechanics [70], whereas mixed states are classical statistical mixtures [71]. Coherence is represented by the off-diagonal elements of the system density matrix, which will be zero for a system in a completely mixed state and nonzero for a system with partial or full coherence. However, as the presence or absence of off-diagonal density matrix elements could be basis dependent, it is always considered more appropriate to check purity as [70,71]

$$\text{Purity} = \text{Tr}(\rho^2), \quad (31)$$

where the bounds of system purity are set such that $1/d \leq \text{Purity} \leq 1$.

The dimension of the associated Hilbert space is denoted by d here. If the system's quantum state is pure ($\text{Purity} = 1$), it spans a one-dimensional subspace of the system Hilbert space [70]. A state that falls within the bounds without being pure or completely mixed ($\text{Purity} = 1/d$) is called a "partially coherent state" [71].

For the excitonic system of our concern, using (31), (19a), (19b), and (19c) it can be shown that

$$\text{Purity} = \frac{1 + \Delta^2}{2} + 2(\mathcal{A}^2 + \mathcal{B}^2) = \frac{1 + \Delta^2}{2} + 2|\rho_{12}|^2. \quad (32)$$

Then the mixedness of the system can be naturally defined as the complement of system purity such that [70] $\text{Mixedness} = 1 - \text{Purity}$. It is important to note that both purity and mixedness are invariant under transformations of

the form $\hat{\rho} \rightarrow \hat{U}\hat{\rho}\hat{U}^\dagger$, where \hat{U} is a unitary operator. For example, this invariance holds under the dynamical mapping $\hat{U}(t, t_0) = e^{-\frac{i}{\hbar}\hat{\mathcal{H}}(t-t_0)}$, where $\hat{\mathcal{H}}$ is the system Hamiltonian [70]. Moreover, when $\mathcal{A}^2, \mathcal{B}^2 \ll 1$ and $\Delta \approx 1$ (32) reduces to $\text{Purity} \approx \frac{1+\Delta^2}{2} \approx \Delta^2 \approx \Delta$. Hence, purity is expected to roughly follow the behavior of Δ under such conditions.

Finally, for comparison purposes, we derive the system purity in the absence of the vicinal MNP. We nullify the effect of the MNP by setting $R \rightarrow \infty$, $T \rightarrow T_0$, and $\tau \rightarrow \tau_0$. Then from (8a) and (8b) $\eta \rightarrow 0$ and $\Omega_{12}^{\text{eff}} \rightarrow \Omega_{12}^0$. This leads to the reduction of the cubic equation (24) to a linear equation with the coefficients $w_1 \rightarrow 4\tau_0 T_0 |\Omega_{12}^0|^2 + T_0^2 \delta^2 + 1$ and $w_0 \rightarrow -T_0^2 \delta^2 - 1$ as $w_2, w_3 \rightarrow 0$. T_0 and τ_0 denote the dephasing and decay rates of the isolated QD, respectively. Substituting these back in (24) yields the steady state analytical population difference of the isolated QD as

$$\Delta_{\text{iqd}} = -\frac{w_0}{w_1} = \frac{T_0^2 \delta^2 + 1}{4T_0 \tau_0 |\Omega_{12}^0|^2 + T_0^2 \delta^2 + 1}. \quad (33)$$

The steady state expressions for the real and imaginary parts of the slowly time varying off-diagonal density matrix element of the isolated QD then become

$$\mathcal{A}_{\text{iqd}} = -\text{Re}\left(\frac{\Omega_{12}^0 \Delta_{\text{iqd}}}{\delta + i/T_0}\right), \quad (34a)$$

$$\mathcal{B}_{\text{iqd}} = \text{Im}\left(\frac{\Omega_{12}^0 \Delta_{\text{iqd}}}{\delta + i/T_0}\right). \quad (34b)$$

Thus,

$$\{\text{Purity}\}_{\text{iqd}} = (1 + \Delta_{\text{iqd}}^2)/2 + 2(\mathcal{A}_{\text{iqd}}^2 + \mathcal{B}_{\text{iqd}}^2). \quad (35)$$

III. SUMMARY OF ANALYTICAL RESULTS

For the convenience of readership, we summarize our GNOR based fully analytical characterization of a QD in the vicinity of an MNP using Table I in the Appendix. Note that when $\delta_{\text{NL}} \rightarrow 0$, the GNOR based nonlocal β of the MNP approaches the Clausius Mossotti factor in the LRA given by [40,50]

$$\beta_{\text{LRA}} = \frac{\epsilon_m(\omega) - \epsilon_b}{\epsilon_m(\omega) + 2\epsilon_b}. \quad (36)$$

Thus, using $\delta_{\text{NL}} \rightarrow 0$, $\tau \rightarrow \tau_0$, and $T \rightarrow T_0$ the conventional LRA based equation set [2,6,34–36,38,50,61,63] can be obtained. Using $R \rightarrow \infty$, $\tau \rightarrow \tau_0$, and $T \rightarrow T_0$, the relevant equations for the isolated QD can be obtained.

IV. RESULTS AND DISCUSSION

Using the presented analytical equations, we study the system behavior over continua of several parameters. Unless specifically mentioned otherwise, the common parameters used for the generated results are as follows: incident field intensity $I_0 = 1 \times 10^3 \text{ W cm}^{-2}$, orientation parameter $s_\alpha = 2$, polarization relaxation (dephasing) time of the isolated QD $T_0 = 0.3 \text{ ns}$, energy or population relaxation time of the isolated QD $\tau_0 = 0.8 \text{ ns}$ [63], dielectric constant of the submerging medium $\epsilon_b = 1$, dielectric constant of the QD material $\epsilon_s = 6$ [63], and QD resonance frequency

TABLE I. Summary of the GNOR based analytical characterization.^{a,b}

QD measure	Expression
Population difference	$\Delta = p_1 + p_2 - \tilde{w}_2/3$, where $p_1 = (\mathcal{P}_1)^{1/3} \in \mathbb{R}$ and $p_2 = (\mathcal{P}_2)^{1/3} \in \mathbb{R}$ for $q^3 + r^2 \geq 0$ $p_1 = \mathcal{P}_1 ^{1/3}[\cos(\theta_1/3) + i \sin(\theta_1/3)]$ and $p_2 = p_1^*$ for $q^3 + r^2 < 0$ $\mathcal{P}_1 = r + \sqrt{q^3 + r^2} = \mathcal{P}_1 \angle \theta_1$ and $\mathcal{P}_2 = r - \sqrt{q^3 + r^2}$, where $q = \tilde{w}_1/3 - \tilde{w}_2^2/9$ and $r = (\tilde{w}_1 \tilde{w}_2 - 3\tilde{w}_0)/6 - \tilde{w}_2^3/27$ $w_3 = T(\omega)^2(\eta_{re}^2 + \eta_{im}^2)$ $\tilde{w}_2 = \{2T(\omega)^2(\omega - \omega_0)\eta_{re} + 2T(\omega)\eta_{im} - w_3\}/w_3$ $\tilde{w}_1 = \{T(\omega)[4\tau(\omega) \Omega_{12}^{eff} ^2 - 2\eta_{im}] + T(\omega)^2[(\omega - \omega_0)^2 - 2\delta\eta_{re}] + 1\}/w_3$ $\tilde{w}_0 = \{-T(\omega)^2(\omega - \omega_0)^2 - 1\}/w_3$ $T = 2\tau t_p/(t_p + 2\tau)$, where $t_p = 2\tau_0 T_0/(2\tau_0 - T_0)$ $\tau = \tau_0/(1 + [f \text{Im}\{\beta(\omega)a^3\}/\{k^3(a+R)^6\}])$, where $k = \omega/c$ $\Omega_{12}^{eff} = [3\mu_d \epsilon_b E_0/2\hbar(2\epsilon_b + \epsilon_s)](1 + s_\alpha \beta a^3/R^3) = \Omega_{re} + i\Omega_{im}$ $\eta = 9s_\alpha^2 \beta a^3 \mu_d^2 \epsilon_b/[4\pi \epsilon_0 \hbar(2\epsilon_b + \epsilon_s)^2 R^6] = \eta_{re} + i\eta_{im}$ $\beta = [\epsilon_m - \epsilon_b(1 + \delta_{NL})]/[\epsilon_m + 2\epsilon_b(1 + \delta_{NL})]$ $\delta_{NL} = [(\epsilon_m - \epsilon_{core})/\epsilon_{core}][j_1(k_L a)/\{k_L a j_1'(k_L a)\}]^c$ $k_L^2 = \epsilon_m/\xi_{GNOR}^2$ $\xi_{GNOR}^2 = \epsilon_{core}[\kappa^2 + D(\gamma - i\omega)]/\{\omega(\omega + i\gamma)\}$ $\kappa^2 = (3/5)v_F^2$ for $\omega \gg \gamma$
Density matrix elements	$\rho_{21} = -(\Omega_{12}^{eff}\Delta)/[(\omega - \omega_0) + \eta\Delta + i/T(\omega)]e^{-i\omega t} = \tilde{\rho}_{21}e^{-i\omega t}$ and $\rho_{12} = \rho_{21}^*$ $\rho_{11} = (1 + \Delta)/2$ and $\rho_{22} = (1 - \Delta)/2$
Normalized Rabi frequency	$\Omega_{12}^r = \Omega_{12}^{eff} + \eta\tilde{\rho}_{21}$
Plasmonic field enhancement	CPFE = $ \Omega_{12}^r(2\hbar\epsilon_{effS})/(\mu_d E_0) ^2$, where $\epsilon_{effS} = (2\epsilon_b + \epsilon_s)/(3\epsilon_b)$
Absorption	$Q_{qd} = \hbar\omega_0\rho_{22}/\tau$
Normalized energy	$\Pi_{21} = \omega_0 - \eta_{re}\Delta$
Normalized dephasing rate	$\Lambda_{21} = 1/T + \eta_{im}\Delta$
Quantum state purity	Purity = $(1 + \Delta^2)/2 + 2 \rho_{12} ^2$
Variables	a = MNP radius v_F = MNP Fermi velocity γ = MNP bulk damping rate D = MNP diffusion constant ϵ_m = MNP dielectric permittivity ϵ_{core} = MNP bound electron response ω_0 = Excitonic resonance (angular) frequency of the isolated QD μ_d = QD transition dipole moment τ_0 = Population relaxation (decay) time of the isolated QD T_0 = Polarization relaxation time of the isolated QD t_p = Pure dephasing time constant of the QD ϵ_s = relative dielectric constant of the QD E_0 = Amplitude of the coherent external illumination ω = Angular frequency of the coherent external illumination R = MNP-QD center separation $s_\alpha = 2, f = 6$ for parallel ($s_\alpha = -1, f = 3/2$ for perpendicular) polarization ϵ_b = relative dielectric constant of the background medium $(c = \text{Speed of light, } \hbar = \text{reduced Planck's constant, } \epsilon_0 = \text{free space permittivity})$

^aUsing $\delta_{NL} \rightarrow 0, \tau \rightarrow \tau_0$ and $T \rightarrow T_0$ the conventional LRA based equation set can be obtained.^bUsing $R \rightarrow \infty$ and $\tau \rightarrow \tau_0$ and $T \rightarrow T_0$, the relevant isolated QD equations can be obtained.^c j_1 is the spherical Bessel function of the first kind of angular-momentum order 1 and j_1' is its first order differential with respect to the argument.

$\omega_0 = 3.5\text{eV}$ [72] such that the QD, MNP, and the incoming coherent radiation are near-resonantly coupled. The analysis uses a silver MNP where the bulk plasma frequency $\hbar\omega_p = 8.99\text{eV}$, bulk damping rate $\hbar\gamma = 0.025\text{eV}$, Fermi velocity $v_f = 1.39 \times 10^6\text{ms}$ [40], diffusion constant $D \approx$

$9.624 \times 10^{-4}\text{m}^2\text{s}^{-1}$ [73], and the experimental bulk dielectric data ϵ_{expt} are obtained from the tabulations by Johnson and Christy [57]. The amplitude E_0 and the intensity I_0 of the coherent external field are related using $E_0 = \sqrt{2I_0/(\epsilon_0 c)}$, where c is the speed of light in vacuum [64].

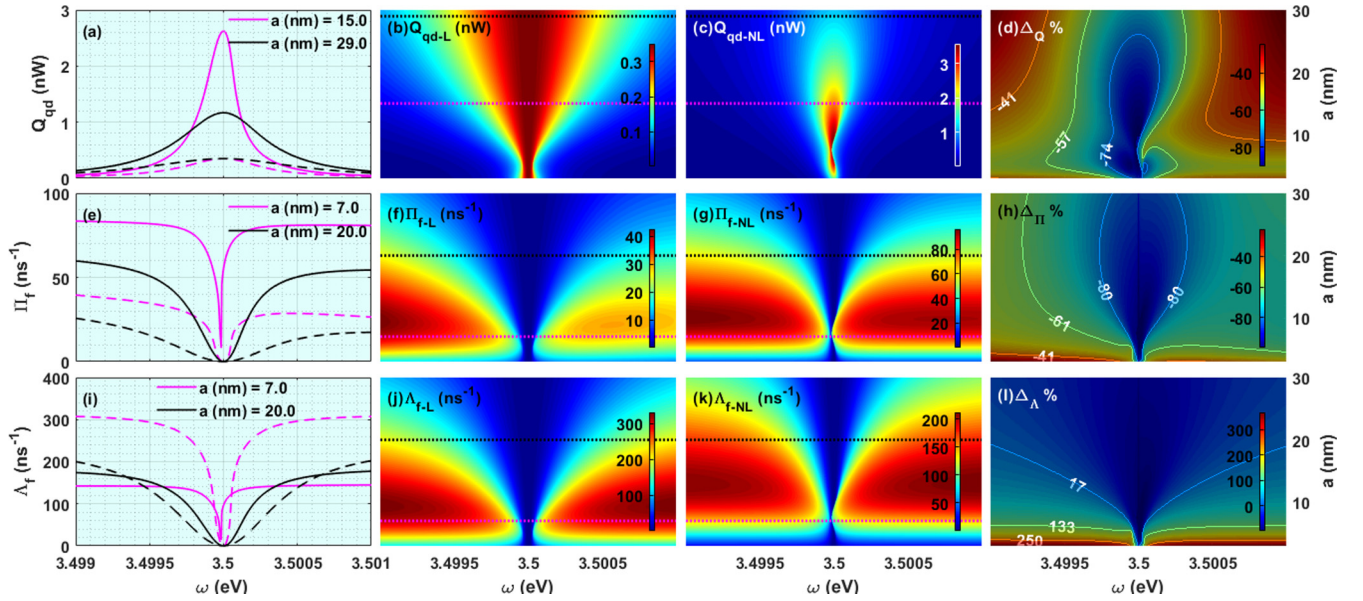


FIG. 2. Second and third columns depict the top view of the $x = \omega$ (range 3.499–3.501 eV), $y = a$ (range 3–30 nm) surface plots of LRA based (subscript L) and the GNOR based (subscript NL) results of Q_{qd} (first row), Π_f (second row), and Λ_f (third row), respectively. The first column depicts the line plots corresponding to the cross sections marked in black and pink on the respective surface plots in the same row. Solid lines represent the GNOR based plots, whereas the dashed lines are the conventional LRA based plots. The final column depicts the signed percentage difference $\Delta_X = (X_L - X_{NL})/X_{NL}\%$, where X denotes the physical quantity of the relevant row. For all subplots, $R = a + 10$ nm and $\mu_d = 1.3e$ nm.

A. Absorption, excitonic energy shift, dephasing rate shift, and plasmonic field enhancement

We first analyze the variation of QD absorption Q_{qd} (in the vicinity of an MNP), MNP induced redshift of the QD excitonic energy Π_f , and MNP induced blueshift of the QD dephasing rate Λ_f with varying MNP radius a and coherent external illumination frequency ω , as depicted in Fig. 2. Subfigures in the second and third columns depict the LRA based and GNOR based results of the three properties, respectively, presented in the form of color-coded surface plots (top view). Subfigures in the first column depict the line plots corresponding to the cross sections indicated in pink and black on the LRA and GNOR based surface plots in the two successive columns of the same row. The solid lines correspond to the GNOR based results, whereas the dashed lines correspond to the relevant LRA based result. The final column shows the surface plots of the percentage difference between the respective LRA and GNOR based results (normalized by the GNOR based result).

Figure 2(a) reveals that Q_{qd} follows a singly peaked distribution along ω (in both LRA and GNOR based models) with a peak near the QD resonance 3.5 eV. It can be observed using Figs. 2(a), 2(b) and 2(c) that the LRA based model suggests smaller peak amplitudes and larger absorption linewidths along the frequency axis compared to the respective GNOR based counterparts. Moreover, as seen in Fig. 2(c), the GNOR model suggests a higher asymmetry of peaks along the frequency axis compared to the LRA based model. The signed percentage difference $\Delta_Q = (Q_{qd-L} - Q_{qd-NL})/Q_{qd-NL}\%$ depicted in Fig. 2(d) reveals that the LRA based model underestimates the QD absorption by more than 23% compared to the GNOR based model, in the entire region under study.

From the second and third rows of Fig. 2, it can be seen that both Π_f and Λ_f possess singly dipped distributions along the ω axis (under both LRA and GNOR based models). From Fig. 2(h), it can be seen that $\Delta_\Pi = (\Pi_{f-L} - \Pi_{f-NL})/\Pi_{f-NL}$ is $< -20\%$ in the entire region under consideration, implying that the LRA based model underestimates the MNP induced redshift of the excitonic resonance frequency by more than 20%. Figure 2(h) indicates that this percentage difference exceeds 80% in magnitude when the external field frequency ω gets close to the bare excitonic resonance ω_0 implying the dominance of nonlocal effects in the region. Figure 2(i) shows that a substantial overestimation of the LRA based Λ_f over the GNOR based result is suggested for MNP radius $a < 10$ nm when the dark blue region with very small detunings from the exciton resonance is exceeded.

We then study the behavior of Q_{qd} , Π_f , and Λ_f when the coherent external field intensity I and the QD dipole moment μ_d are varied in continua, using Fig. 3. All subplots are in the same constellation as Fig. 2. From Fig. 3(d) it is evident that $\Delta_Q = (Q_L - Q_{NL})/Q_{NL}\% < -40\%$ in the entire region, suggesting that the LRA based model underestimates the QD absorption compared to the case where the nonlocal effects are taken into account. It can also be observed that this percentage difference is almost invariant along the I axis for a given value of μ_d .

From the second and third rows of Fig. 3, it can be seen that both Π_f and Λ_f are almost invariant along the I axis for a given μ_d . Figure 3(h) shows that $\Delta_\Pi = (\Pi_{f-L} - \Pi_{f-NL})/\Pi_{f-NL}\% < -14\%$ in the entire parameter region suggesting that the GNOR based model results in higher redshifts to the exciton resonance when in the near field of an MNP. From Fig. 3(i) it is evident that the GNOR based model suggests smaller blueshifts to the QD dephasing

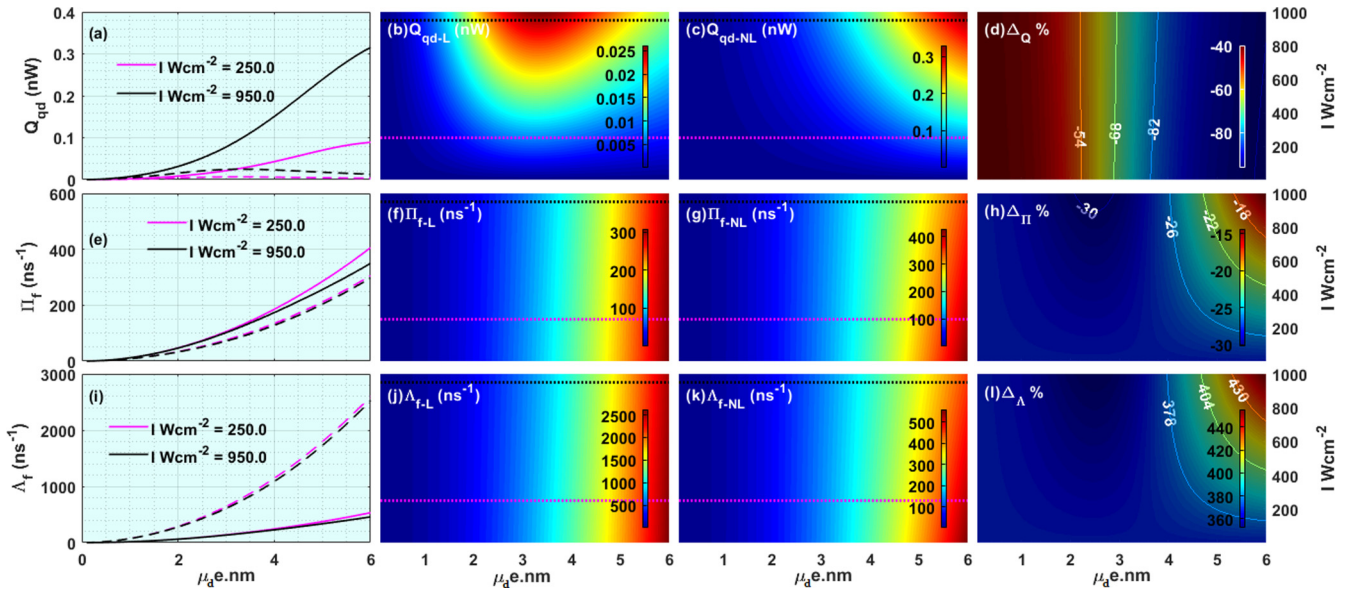


FIG. 3. Second and third columns depict the top view of the $x = \mu_d$, $y = I$ surface plots of LRA based (subscript L) and the GNOR based (subscript NL) results of the QD energy absorption Q_{qd} (first row), excitonic energy (red) shift Π_f (second row), and dephasing rate (blue) shift Λ_f (third row), respectively. The first column depicts the line plots corresponding to the cross sections marked in black and pink on the respective surface plots in the same row. Solid lines represent the GNOR based plots, whereas the dashed lines are the conventional LRA based plots. The final column depicts the signed percentage difference $\Delta_X = (X_L - X_{NL})/X_{NL}\%$, where X denotes the physical quantity of the relevant row. For all subplots, the MNP radius $a = 3$ nm, MNP-QD center separation $R = 13$ nm, and frequency of the coherent external illumination $\omega = 3.4995$ eV.

compared to the LRA based model, resulting in $\Delta_\Lambda = (\Lambda_{f-L} - \Lambda_{f-NL})/\Lambda_{f-NL} > 350\%$ in the entire region under consideration.

In Fig. 4 we study the variation of coherent plasmonic field enhancement (CPFE) experienced by the QD, Π_f , and Λ_f when μ_d and ω are varied, using the usual arrangement of subfigures. The first row depicts the LRA and GNOR based predictions (both as line and surface plots) of CPFE and their percentage difference. From Figs. 4(a)–4(c) it can be observed that the GNOR based model suggests a Fano-like distribution for CPFE, whereas the LRA based model suggests a modified Fano-like distribution. From Fig. 4(d) it is evident that the GNOR based model entails significant modification of CPFE from the LRA based model as μ_d increases and the detuning of ω from ω_0 decreases. The second and third rows of Fig. 4 correspond to Π_f and Λ_f , respectively, both of which follow narrow, singly dipped frequency distributions for all μ_d , under both LRA and GNOR based models. In line with the observations in the earlier parameter spaces, the GNOR model suggests higher redshifts (Π_f) to the exciton resonance in the entire parameter region. It suggests lower blueshifts (Λ_f) to the QD dephasing rate compared to the LRA based model, except at coherent illumination frequencies extremely close to ω_0 .

B. Analysis of the near PMR region

We then study the behavior of the QD as the MNP-QD center separation (R) and the QD dipole moment (μ_d) are varied. The first, second, and third rows of Fig. 5 correspond to the real component of the normalized QD Rabi frequency

$\text{Re}[\Omega'_{12}]$, the QD population difference Δ , and QD absorption Q_{qd} in the usual arrangement of subplots.

The solid lines of Fig. 5(a) which correspond to the GNOR based prediction have four distinguishable features, especially when $\mu_d > 1$ nm. (i) For large R , it can be seen that $\text{Re}[\Omega'_{12}] \rightarrow \Omega_{12}^0$, and the field experienced by the QD approaches the externally applied field. (ii) $\text{Re}[\Omega'_{12}]$, and hence the field experienced by the QD slightly increases above Ω_{12}^0 as R decreases. (iii) This enhancement reaches a peak and then starts to decrease with further decrease of R , which is an indication of the competition between Förster energy transfer from QD to MNP and the plasmonic field enhancement near QD. (iv) This follows by an encounter of an abrupt and significant decrease of $\text{Re}[\Omega'_{12}]$, and hence the field experienced by the QD, as R decreases further. This could be identified as near PMR (plasmonic meta resonance)-like behavior of the MNP-QD hybrid nanosystem [6]. PMR corresponds to a “molecular-type” resonance which is quite different from the conventional atomic resonances. It occurs under strong exciton-plasmon coupling, when separately distinguishable bright and dark states are experienced by the QD. The dark state which corresponds to dramatic screening of the effective field experienced by the QD, due to the presence of the MNP, is an indication of the PMR. PMR-like behavior of MNP-QD nanostructures has recently been under study for a multitude of practical applications such as in-vivo nanoscale switching [6,7].

Juxtaposition of Figs. 5(c), 5(g) and 5(k) reveal that the dip in the distribution of Δ along R axis and the corresponding peak of Q_{qd} coincide with the relevant PMR related dip along the R axis in (c) for $\mu_d > 1$ nm. Moreover, the percentage difference plots [Figs. 5(d), 5(h) and 5(l)] indicate that both

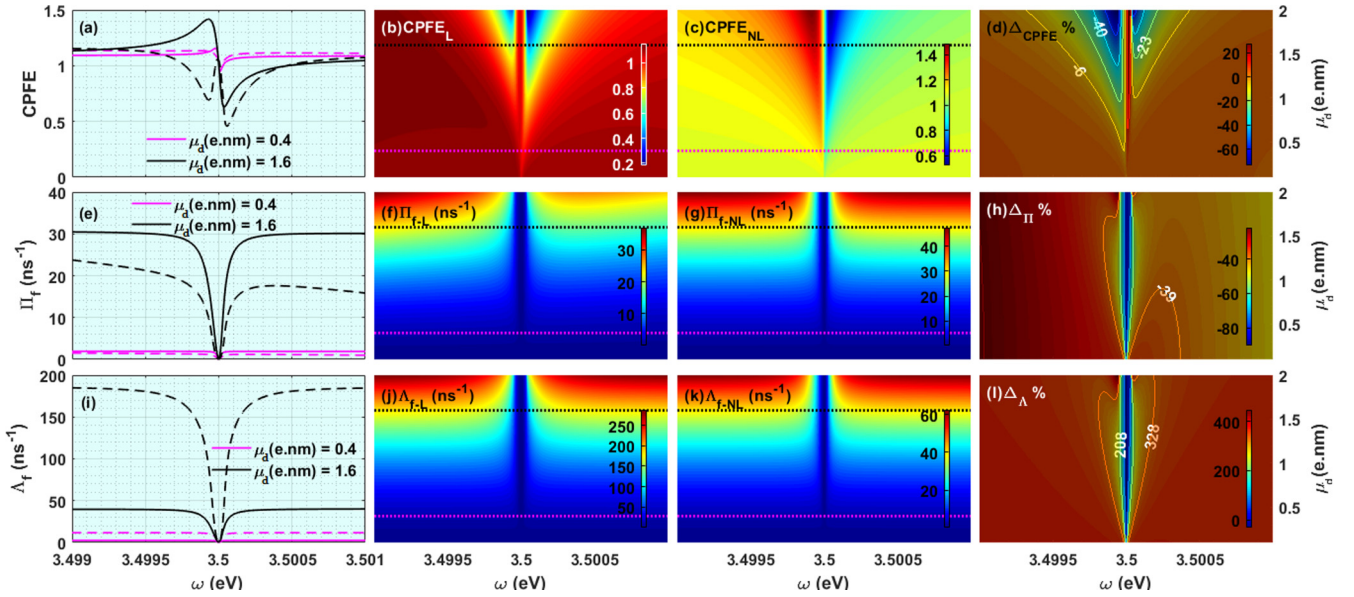


FIG. 4. Second and third columns depict the top view of the $x = \omega$, $y = \mu_d$ surface plots of LRA based (subscript L) and the GNOR based (subscript NL) results of CPFE (first row), Π_f (second row), and Δ_f (third row), respectively. The first column depicts the line plots corresponding to the cross sections marked in black and pink on the respective surface plots in the same row. Solid lines represent the GNOR based plots, whereas the dashed lines are the conventional LRA based plots. The final column depicts the signed percentage difference $\Delta_X = (X_L - X_{NL})/X_{NL}\%$, where X denotes the physical quantity of the relevant row. For all subplots, $a = 3$ nm, $R = 13$ nm.

LRA and GNOR based models converge towards the same values when R exceeds 30 nm.

C. Population difference and quantum state purity

We then study the resemblance of QD population difference Δ to its quantum state purity using Fig. 6. In this figure, Figs. 6(b), 6(c), and 6(d) in the first row depict the

variation of the LRA based (Δ_L), GNOR based (Δ_{NL}), and the isolated QD (Δ_{qd}) population differences, respectively, with varying ω and μ_d . Figure 6(a) depicts the line plots corresponding to the cross sections marked in pink and black on the three subsequent surface plots. The solid, dashed, and dotted-dashed lines correspond to the GNOR based, LRA based, and the isolated QD cases, respectively. Figure 6(e)

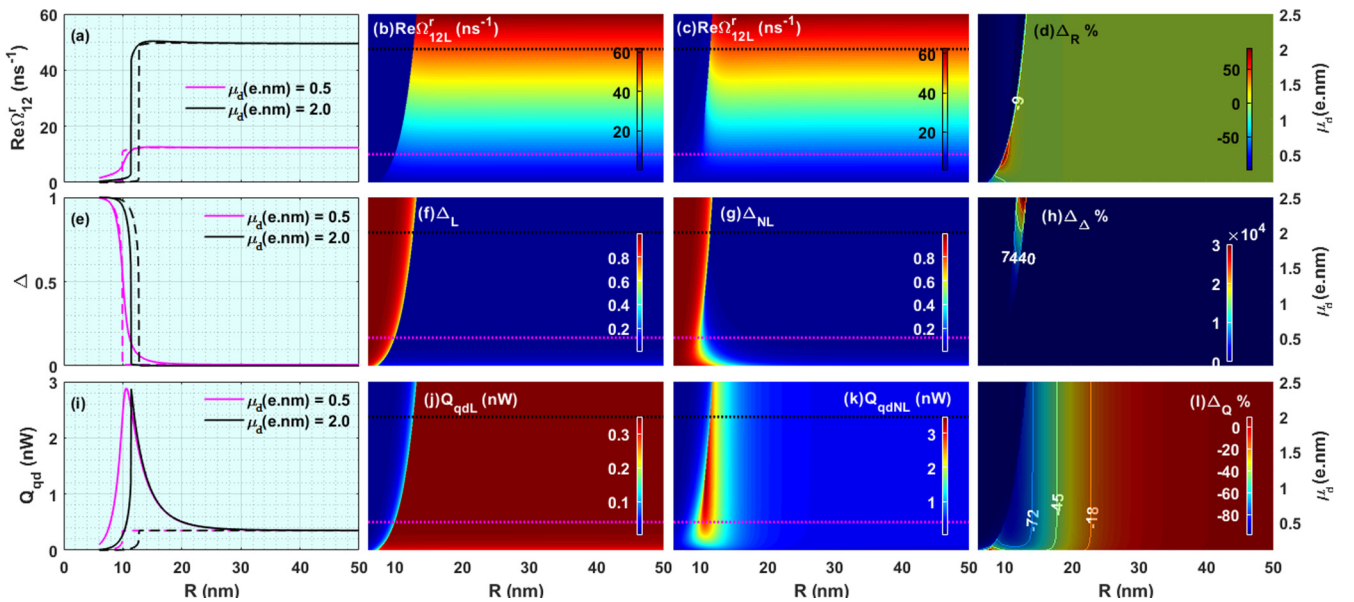


FIG. 5. Second and third columns depict the top view of the $x = R$, $y = \mu_d$ surface plots of LRA based (subscript L) and the GNOR based (subscript NL) results of $\text{Re } \Omega_{12}^r$ (first row), Δ (second row), and Q_{qd} (third row), respectively. The first column depicts the line plots corresponding to the cross sections marked in black and pink on the respective surface plots in the same row. Solid lines represent the GNOR based plots, whereas the dashed lines are the conventional LRA based plots. The final column depicts the signed percentage difference $\Delta_X = (X_L - X_{NL})/X_{NL}\%$, where X denotes the physical quantity of the relevant row. For all subplots $a = 3$ nm, $\omega = \omega_0$.

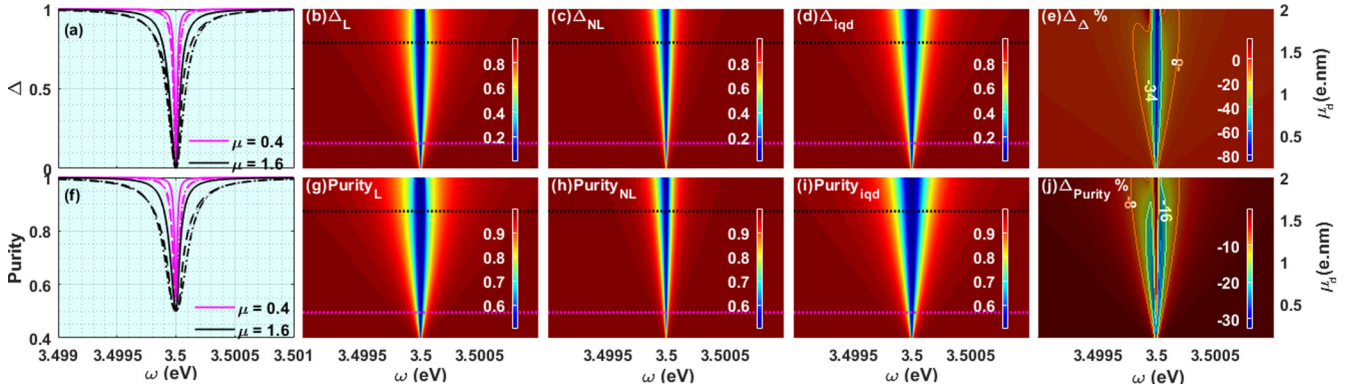


FIG. 6. Second, third, and fourth columns depict the top view of the $x = \omega$, $y = \mu_d$ surface plots of LRA based (subscript L) and the GNOR based (subscript NL) and isolated QD (subscript iqd) results of Δ (first row) and Purity, respectively. The first column depicts the line plots corresponding to the cross sections marked in black and pink on the respective surface plots in the same row. Solid lines represent the GNOR based plots, whereas the dashed lines are the conventional LRA based plots and the dotted-dashed lines are the isolated QD plots. The final column depicts the signed percentage difference $\Delta_X = (X_L - X_{NL})/X_{NL}\%$, where X denotes the physical quantity of the relevant row. For all subplots, $a = 3$ nm, $R = 13$ nm.

shows the usual surface-contour plot of the LRA and GNOR percentage difference $\Delta_\Delta = (\Delta_L - \Delta_{NL})/\Delta_{NL}\%$. The second row of Fig. 6 depicts the same constellation of subplots as the preceding row, for the quantum state purity of the QD.

Comparison of the first row to the corresponding plots of the second reveals that the plot shapes of population difference bear a high resemblance to the respective quantum state purity plots. It can also be observed that when $\Delta \rightarrow 1$, Purity $\rightarrow \Delta$ suggesting the existence of the QD in a completely pure state where the state occupation probabilities, $\rho_{11} \rightarrow 1$ and $\rho_{22} \rightarrow 0$. In contrast, when $\Delta \rightarrow 0$, Purity $\rightarrow 0.5$ (the minimum possible value of purity of a two state system) suggesting that $\rho_{11} \rightarrow 0.5$ and $\rho_{22} \rightarrow 0.5$, leading the QD to a completely mixed state. Observation of the first three subplots of each row reveals that both Δ and Purity possess singly dipped frequency distributions for each value of μ_d where $\Delta \rightarrow 0$ (and Purity $\rightarrow 0.5$) when the detuning of the external field with the QD resonance decreases, for all three cases under study. The isolated QD spectra for Δ and Purity exhibit a symmetric dip near ω_0 which constantly broadens with increasing μ_d . The LRA based model suggests a symmetric dip around ω_0 , the broadening of which is lesser than that of the isolated QD case, towards higher values of μ_d . In contrast, the GNOR based model suggests a dip around ω_0 with growing asymmetry as μ_d increases. Figure 6(e) indicates that the percentage difference between the LRA and GNOR based Δ predictions become significant as the detuning of the external field (with respect to ω_0) decreases. Δ and Purity values from both models tend to coincide at high detunings from ω_0 .

D. Comparison between HDM and GNOR

Finally, we perform a comparison between HDM based and the proposed GNOR based characterizations of the QD influenced by a near-field MNP. Figure 7 depicts sample results of the comparison. It is evident that the observed differences are quite significant for MNP radii less than 10 nm, where the experimentally observed size dependent resonance shifts of metal nanoparticles (attributed to nonlocal effects) are most significant [44]. The differences observed between the HDM

and GNOR based results mainly arise as the GNOR model accounts for the electron diffusion phenomenon in the MNP which arises mainly due to surface effects such as Landau damping [40]. From a similar analysis in the μ_d vs R space, it was observable that the difference between HDM and GNOR based results are significant near the PMR-like region and both models tend to give similar predictions when R increases beyond 30 nm (when $a = 3$ nm), due to the decreased impact of the MNP.

E. Summary of physical observations

Using the above results and discussion, we can conclude that the GNOR based characterization of a QD exciton situated in the near field of an MNP displays higher levels of energy absorption (Q_{qd}), compared to its LRA based counterpart, at least in the large parameter space under study. It also suggests steeper spectral linewidths along the frequency axis for Q_{qd} and larger MNP induced redshifts (Π_f) to the excitonic resonance frequency compared to the LRA based model. The following interesting phenomena (left unrevealed by the LRA based model) were also displayed by the proposed GNOR based model, in the selected parameter regime. It suggests a Fano-like spectrum near the bare excitonic resonance for the coherent plasmonic field enhancement (CPFE) experienced by the QD and plasmonic meta resonancelike behavior towards small values of MNP-QD center separation R . Moreover, incorporation of the nonlocal effects introduces an asymmetry to the dips of QD population Δ and quantum state purity near the bare excitonic resonance ω_0 .

In summary, the proposed GNOR based model predicts strong modifications to various QD properties such as population difference, absorption, MNP induced shifts to excitonic energy and Förster enhanced broadening, coherent plasmonic field enhancement, and quantum state purity, compared to the conventional LRA based predictions. Such modifications are prominent with small MNP radii, high QD dipole moments, small detunings (of the coherent external illumination from the bare excitonic resonance), and near parameter regions exhibiting plasmonic meta resonance (PMR)-like behavior, implying the dominance of nonlocal effects in such regions.

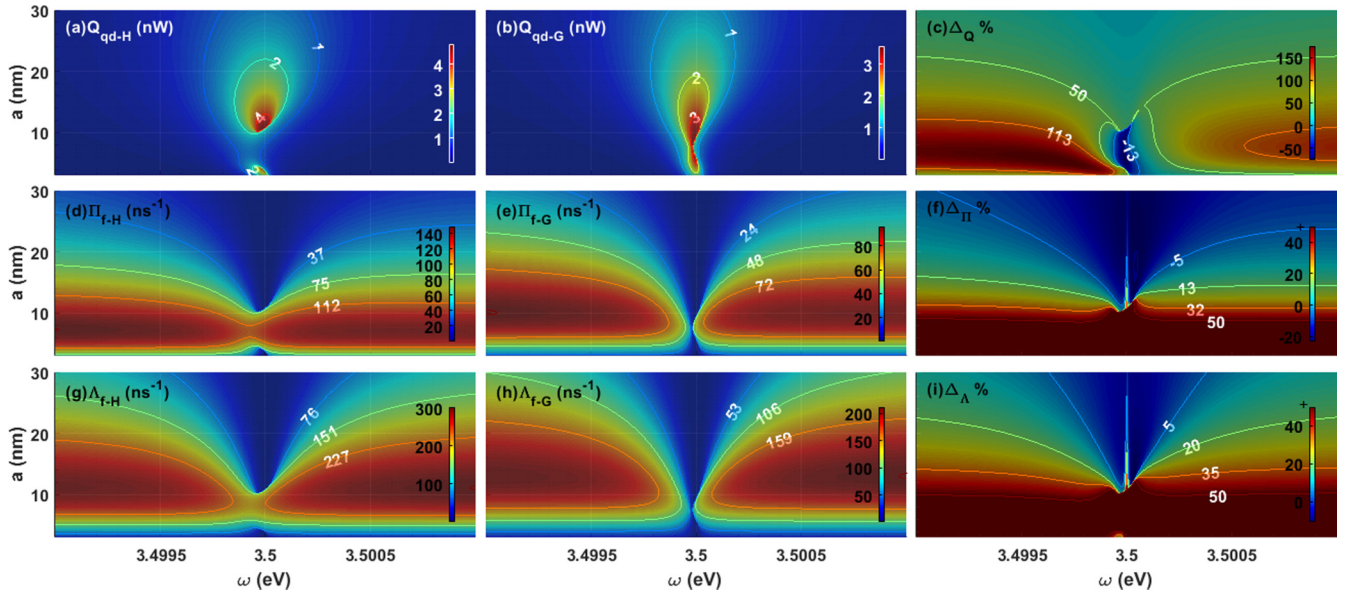


FIG. 7. Comparison of sample HDM and GNOR based results. Figures depict the top view of the $x = \omega$ (range 3.499–3.501 eV), $y = a$ (range 3–30 nm) surface plots of HDM based (subscript H) and the GNOR based (subscript G) results of Q_{qd} (first row), Π_f (second row), and Λ_f (third row), respectively. The final column depicts the signed percentage difference $\Delta_X = (X_H - X_G)/X_G\%$, where X denotes the physical quantity of the relevant row. For all subplots, $R = a + 10$ nm and $\mu_d = 1.3$ e nm.

V. CONCLUSION

In this paper we analytically studied the influence of a metal nanoparticle (MNP) situated in the near field, on the behavioral trends of an exciton in a quantum dot (QD) using a generalized nonlocal optical response (GNOR) method based approach. It has been shown in literature that the GNOR model allows unified theoretical explanation of experimentally observed plasmonic phenomena such as the size dependent resonance shifts of metal nanoparticles that previously seemed to require *ab initio* microscopic theory, as the conventional local response approximation fails to reveal them. We believe that our improved analytical model will facilitate gaining better physical intuition of the simple yet powerful nanohybrid under study and would also enable application specific parameter optimization. We used the analytical model to peruse the system over a wide parameter range, taking the nonlocal response of the MNP into account, at a much lesser level of complexity compared to the local response approximation based numerical methods or *ab initio* approaches of accounting for the nonlocal effects. We tabulated the GNOR based fully analytical characterization of a QD in the vicinity of an MNP, with the guidance to retrieve the conventional local response approximation (LRA) based and isolated QD related equations, for the easy reference by readership. Using the newly suggested model, we predicted that MNP radius and QD dipole moment dependent differences exist between the spectra obtained using the GNOR based and conventional LRA based methods for quantities such as the MNP induced redshift of normalized excitonic energy, Förster-enhanced broadening of the excitonic transition, absorption rate, quantum state purity, etc. of a QD when it is perturbed by a vicinal MNP. Moreover, these differences are quite significant for

QDs with high dipole moments located near small MNPs, at the incidence of illumination sparsely detuned from the bare excitonic resonance as well as near the parameter regions exhibiting plasmonic meta resonance (PMR)-like behavior which have recently been under study for a multitude of practical applications such as nanoscale switching. Based on our results it can be suggested that the effects of nonlocal response non-negligibly affects the near field QD even in ranges where MNP radius is few tens of nanometers and hence is important to be accounted for in the entire quasistatic regime. It could also be observed that the LRA and GNOR based results tend to converge when the interparticle distance far exceeds the plasmonic meta resonant region, as expected.

ACKNOWLEDGMENTS

H.H. gratefully acknowledges the encouragement and support by D. U. Kudavithana and all members of A χ L at Monash University including S. Mallawaarachchi. The work of H.H. is supported by the Monash University Institute of Graduate Research.

APPENDIX: ROOT SELECTION FOR $q^3 + r^2 < 0$

As summarized in Table I, for $q^3 + r^2 < 0$, \mathcal{P}_1 and \mathcal{P}_2 from (27) will be complex conjugates such that

$$\mathcal{P}_1 = r + \sqrt{q^3 + r^2} = |\mathcal{P}_1|/\theta_1,$$

$$\mathcal{P}_2 = r - \sqrt{q^3 + r^2} = |\mathcal{P}_1|/-\theta_1.$$

It is evident that (26) mandates p_1 and p_2 to be complex conjugates of each other for at least one cubic root of (25) to be real. Thus, using De Moivre's n th root theorem for complex

numbers [74] and trigonometric identities, it can be shown that

$$\begin{aligned} \mathcal{P}_1^{1/3}(j) &= |\mathcal{P}_1|^{1/3} \left[\cos\left(\frac{\theta_1}{3} + \frac{2j\pi}{3}\right) + i \sin\left(\frac{\theta_1}{3} + \frac{2j\pi}{3}\right) \right] \\ &= |\mathcal{P}_2|^{1/3} \left[\cos\left(\frac{\theta_1}{3} + \frac{2(-j)\pi}{3}\right) - i \sin\left(\frac{\theta_1}{3} + \frac{2(-j)\pi}{3}\right) \right] \\ &= [\mathcal{P}_2^{1/3}(-j)]^*, \end{aligned}$$

where $j = 0, 1, 2$.

Comparison of all possibilities of the roots of (25) against its steady state numerical solution over the large parameter space used in this work reveals that the valid root for $-1 \leq \Delta \leq 1$ when $q^3 + r^2 < 0$ is given by

$$\Delta = p_1 + p_2 - \tilde{w}_2/3,$$

where

$$\begin{aligned} p_1 &= \mathcal{P}_1^{1/3}(j=0) = |\mathcal{P}_1|^{1/3} \left[\cos\left(\frac{\theta_1}{3}\right) + i \sin\left(\frac{\theta_1}{3}\right) \right], \\ p_2 &= p_1^*. \end{aligned}$$

-
- [1] K. E. Sapsford, T. Pons, I. L. Medintz, and H. Mattoussi, *Sensors* **6**, 925 (2006).
- [2] A. Hatef, S. M. Sadeghi, S. Fortin-Deschênes, E. Boulais, and M. Meunier, *Opt. Express* **21**, 5643 (2013).
- [3] M. Toishi, D. Englund, A. Faraon, and J. Vučković, *Opt. Express* **17**, 14618 (2009).
- [4] D. Weeraddana, M. Premaratne, and D. L. Andrews, *Phys. Rev. B* **92**, 035128 (2015).
- [5] D. Weeraddana, M. Premaratne, S. D. Gunapala, and D. L. Andrews, *J. Chem. Phys.* **147**, 074117 (2017).
- [6] S. Sadeghi, *Nanotechnology* **21**, 355501 (2010).
- [7] S. Sadeghi, in *Plasmonics: Metallic Nanostructures and Their Optical Properties XIII*, Vol. 9547 (International Society for Optics and Photonics, Bellingham, WA, 2015), p. 95473D.
- [8] W. Zhu, I. D. Rukhlenko, and M. Premaratne, *Appl. Phys. Lett.* **101**, 031907 (2012).
- [9] M. Noginov, G. Zhu, A. Belgrave, R. Bakker, V. Shalae, E. Narimanov, S. Stout, E. Herz, T. Suteewong, and U. Wiesner, *Nature (London)* **460**, 1110 (2009).
- [10] T. Warnakula, M. I. Stockman, and M. Premaratne, *J. Opt. Soc. Am. B* **35**, 1397 (2018).
- [11] L. Kumarapperuma, M. Premaratne, P. K. Jha, M. I. Stockman, and G. P. Agrawal, *Appl. Phys. Lett.* **112**, 201108 (2018).
- [12] C. Jayasekara, M. Premaratne, M. I. Stockman, and S. D. Gunapala, *J. Appl. Phys.* **118**, 173101 (2015).
- [13] C. Jayasekara, M. Premaratne, S. D. Gunapala, and M. I. Stockman, *J. Appl. Phys.* **119**, 133101 (2016).
- [14] C. K. W. Jayasekara, M. Premaratne, S. D. Gunapala, and M. Stockman, in *CLEO: QELS Fundamental Science* (Optical Society of America, Washington, DC, 2016), pp. FTu1B-2.
- [15] B. Liu, W. Zhu, S. D. Gunapala, M. I. Stockman, and M. Premaratne, *ACS Nano* **11**, 12573 (2017).
- [16] S. Sadeghi, *Nanotechnology* **21**, 455401 (2010).
- [17] S. M. Sadeghi, *Phys. Rev. B* **82**, 035413 (2010).
- [18] S. Pang, R. E. Beckham, and K. E. Meissner, *Appl. Phys. Lett.* **92**, 221108 (2008).
- [19] T. Nakamura, T. Asano, K. Kojima, T. Kojima, and S. Noda, *Phys. Rev. B* **84**, 245309 (2011).
- [20] K. Hennessy, A. Badolato, M. Winger, D. Gerace, M. Atatüre, S. Gulde, S. Fält, E. L. Hu, and A. Imamoglu, *Nature (London)* **445**, 896 (2007).
- [21] M. Premaratne and G. P. Agrawal, *Light Propagation in Gain Media: Optical Amplifiers* (Cambridge University Press, Cambridge, 2011), Chap. 4-4, pp. 96-97.
- [22] S. A. Maier, *Plasmonics: Fundamentals and Applications* (Springer Science & Business Media, 2007).
- [23] M. I. Stockman, *Opt. Express* **19**, 22029 (2011).
- [24] H. P. Hapuarachchi, S. Mallawaarachchi, H. T. Hattori, W. Zhu, and M. Premaratne, *J. Phys.: Condens. Matter* **30**, 054006 (2018).
- [25] D. Sikdar and A. A. Kornyshev, *Sci. Rep.* **6**, 33712 (2016).
- [26] Y. Liu, X. Dai, S. Mallawaarachchi, H. Hapuarachchi, Q. Shi, D. Dong, S. H. Thang, M. Premaratne, and W. Cheng, *J. Mater. Chem. C* **5**, 10926 (2017).
- [27] C. S. Kumarasinghe, M. Premaratne, Q. Bao, and G. P. Agrawal, *Sci Rep.* **5**, 12140 (2015).
- [28] C. S. Kumarasinghe, M. Premaratne, S. D. Gunapala, and G. P. Agrawal, *Sci Rep.* **6**, 21470 (2016).
- [29] C. S. Kumarasinghe, M. Premaratne, and G. P. Agrawal, in *European Quantum Electronics Conference* (Optical Society of America, Washington, DC, 2015), p. EG_5b_3.
- [30] D. Sikdar, I. D. Rukhlenko, W. Cheng, and M. Premaratne, *Plasmonics* **9**, 659 (2014).
- [31] D. Sikdar, I. D. Rukhlenko, W. Cheng, and M. Premaratne, *Biomed. Opt. Express* **4**, 15 (2013).
- [32] W. Zhu, I. D. Rukhlenko, and M. Premaratne, *J. Opt. Soc. Am. B* **29**, 2659 (2012).
- [33] M. Achermann, *J. Phys. Chem. Lett.* **1**, 2837 (2010).
- [34] G. W. Bryant, R. D. Artuso, A. Garcia-Etxarri, and J. Aizpurua, in *Quantum Electronics and Laser Science Conference* (Optical Society of America, Washington, DC, 2011), p. QThL3.
- [35] R. D. Artuso and G. W. Bryant, *Nano Lett.* **8**, 2106 (2008).
- [36] R. D. Artuso and G. W. Bryant, *Phys. Rev. B* **82**, 195419 (2010).
- [37] W. Zhang, A. O. Govorov, and G. W. Bryant, *Phys. Rev. Lett.* **97**, 146804 (2006).
- [38] S. Sadeghi, *Nanotechnology* **20**, 225401 (2009).
- [39] S. Sadeghi, in *Frontiers in Biological Detection: From Nanosensors to Systems V* (International Society for Optics and Photonics, Bellingham, WA, 2013), Vol. 8570, p. 85700J.
- [40] S. Raza, S. I. Bozhevolnyi, M. Wubs, and N. A. Mortensen, *J. Phys.: Condens. Matter* **27**, 183204 (2015).
- [41] M. Wubs and N. A. Mortensen, *Nonlocal Response in Plasmonic Nanostructures* (Springer, Berlin, 2017), Chap. 12.

- [42] J. Tiggesbäumker, L. Köller, K.-H. Meiwes-Broer, and A. Liebsch, *Phys. Rev. A* **48**, R1749 (1993).
- [43] S. Raza, N. Stenger, S. Kadkhodazadeh, S. V. Fischer, N. Kostesh, A.-P. Jauho, A. Burrows, M. Wubs, and N. A. Mortensen, *Nanophotonics* **2**, 131 (2013).
- [44] S. Raza, W. Yan, N. Stenger, M. Wubs, and N. A. Mortensen, *Opt. Express* **21**, 27344 (2013).
- [45] C. Kumarasinghe, M. Premaratne, and G. P. Agrawal, *Opt. Express* **22**, 11966 (2014).
- [46] C. S. Kumarasinghe, M. Premaratne, S. D. Gunapala, and G. P. Agrawal, *Phys. Chem. Chem. Phys.* **18**, 18227 (2016).
- [47] J. Zuloaga, E. Prodan, and P. Nordlander, *Nano Lett.* **9**, 887 (2009).
- [48] K. Andersen, K. W. Jacobsen, and K. S. Thygesen, *Phys. Rev. B* **86**, 245129 (2012).
- [49] N. A. Mortensen, S. Raza, M. Wubs, T. Søndergaard, and S. I. Bozhevolnyi, *Nat. Commun.* **5**, 3809 (2014).
- [50] R. D. Artuso, *The Optical Response of Strongly Coupled Quantum Dot-Metal Nanoparticle Hybrid Systems* (University of Maryland, College Park, 2012).
- [51] V. Brázdová and D. R. Bowler, *Atomistic Computer Simulations: A Practical Guide* (John Wiley & Sons, New York, 2013).
- [52] R. Esteban, A. G. Borisov, P. Nordlander, and J. Aizpurua, *Nat. Commun.* **3**, 825 (2012).
- [53] M. Premaratne and M. I. Stockman, *Adv. Opt. Photon.* **9**, 79 (2017).
- [54] H. Hapuarachchi, M. Premaratne, Q. Bao, W. Cheng, S. D. Gunapala, and G. P. Agrawal, *Phys. Rev. B* **95**, 245419 (2017).
- [55] S. Mallawaarachchi, M. Premaratne, S. D. Gunapala, and P. K. Maini, *Phys. Rev. B* **95**, 155443 (2017).
- [56] S. Mallawaarachchi, S. D. Gunapala, M. I. Stockman, and M. Premaratne, *Phys. Rev. B* **97**, 125406 (2018).
- [57] P. B. Johnson and R.-W. Christy, *Phys. Rev. B* **6**, 4370 (1972).
- [58] D. Weeraddana, M. Premaratne, and D. L. Andrews, *Phys. Rev. B* **93**, 075151 (2016).
- [59] D. Weeraddana, M. Premaratne, S. D. Gunapala, and D. L. Andrews, *Phys. Rev. B* **94**, 085133 (2016).
- [60] A. Ridolfo, O. Di Stefano, N. Fina, R. Saija, and S. Savasta, *Phys. Rev. Lett.* **105**, 263601 (2010).
- [61] A. Hatef, S. Sadeghi, and M. R. Singh, *Nanotechnology* **23**, 205203 (2012).
- [62] P. Meystre and M. Sargent, *Elements of Quantum Optics* (Springer Science & Business Media, New York, 2013), Chap. 3, p. 79.
- [63] R. Artuso and G. Bryant, *Acta Phys. Pol. A* **122**, (2012).
- [64] S. G. Kosionis, A. F. Terzis, V. Yannopoulos, and E. Paspalakis, *J. Phys. Chem. C* **116**, 23663 (2012).
- [65] J. Vielma and P. Leung, *J. Chem. Phys.* **126**, 194704 (2007).
- [66] P. Leung, *Phys. Rev. B* **42**, 7622 (1990).
- [67] H. Grant and I. Kleiner, *Turning Points in the History of Mathematics* (Birkhäuser, Basel, Switzerland, 2016), Chap. 2.
- [68] B. Thorgrimsson, D. Kim, Y.-C. Yang, L. W. Smith, C. B. Simmons, D. R. Ward, R. H. Foote, J. Corrigan, D. E. Savage, M. G. Lagally *et al.*, *npj Quantum Inf.* **3**, 32 (2017).
- [69] D. Loss and D. P. DiVincenzo, *Phys. Rev. A* **57**, 120 (1998).
- [70] G. Jaeger, *Quantum Information* (Springer, Berlin, 2007).
- [71] D. McMahon, *Quantum Mechanics Demystified* (McGraw-Hill, New York, 2013).
- [72] D. O. Demchenko and L.-W. Wang, *Phys. Rev. B* **73**, 155326 (2006).
- [73] S. Raza, M. Wubs, S. I. Bozhevolnyi, and N. A. Mortensen, *Opt. Lett.* **40**, 839 (2015).
- [74] C. Y. Young, *Trigonometry* (John Wiley & Sons, New York, 2011).